

# Heating and cooling in self-consistent many-body simulations

Yang Yu,<sup>1</sup> Sergei Isakov,<sup>1</sup> and Emanuel Gull<sup>1</sup>

<sup>1</sup>*Department of Physics, University of Michigan, Ann Arbor, MI 48109, USA*

(Dated: June 18, 2024)

We present a temperature extrapolation technique for self-consistent many-body methods, which provides a causal starting point for converging to a solution at a target temperature. The technique employs the Carathéodory formalism for interpolating causal matrix-valued functions and is applicable to various many-body methods, including dynamical mean field theory, its cluster extensions, and self-consistent perturbative methods such as the self-consistent GW approximation. We show results that demonstrate that this technique can efficiently simulate heating and cooling hysteresis at a first-order phase transition, as well as accelerate convergence.

## I. INTRODUCTION

When conducting experiments in condensed matter physics, it is common practice to investigate the temperature dependence of observables while keeping other parameters constant. A particular example are specific heat or transport measurements, which are often used as a preliminary probe to identify intriguing temperature-dependent behavior. For example, in a first-order coexistence regime, heating and cooling curves may reveal history-dependent hysteresis.

In theoretical calculations using self-consistent finite-temperature field theories, changing the temperature of a system is generally not practical as it causes a shift of Matsubara frequencies [1, 2]. Extrapolating the lowest Matsubara frequency during cooling can be problematic, resulting in non-causal solutions. Therefore, implementing heating and cooling protocols in self-consistent finite-temperature field theories, in analogy to heating and cooling measurements in experiment, is an unresolved issue.

Self-consistent finite-temperature simulation methods include non-perturbative techniques, such as the dynamical mean field theory (DMFT) [3] and its cluster variants [4–7]; self-consistent perturbative methods, such as GW [8–13], second-order perturbation theory [14–17], fluctuation-exchange or T-matrix approximations [18, 19], as well as bold-line diagrammatic Monte Carlo methods [20–23]; and combinations of embedding theories with perturbation theory [24–26].

In these methods, solutions are obtained through an iterative process that involves starting with an initial guess and continuing the process until self-consistency is achieved. The number of iterations required to reach convergence is directly related to how close the starting point is to the iteration fixed point. A ‘good’ starting point can significantly reduce the computational effort required for the simulation, whereas a ‘bad’ starting point may result in iterations that diverge, iterate in limit cycles, or even converge to unphysical fixed points [27]. In parameter regimes where first-order coexistence occurs, multiple physical fixed points may exist [28–32].

This paper addresses the challenge of generating better starting points and implementing heating and cool-

ing protocols in self-consistent many-body methods. It presents a solution that guarantees a causal starting point by using a converged solution at a different temperature. The proposed method relies on the Carathéodory formalism [33] for interpolating causal matrix-valued functions. Originally developed for analytic continuation of matrix-valued Matsubara functions to real frequencies, this formalism can be extended to temperature extrapolation, which involves evaluating an interpolant at different Matsubara frequencies. We demonstrate the effectiveness of this approach in obtaining improved starting points in the context of DMFT and real-materials perturbation theory. Additionally, we examine heating and cooling hysteresis in the context of a first-order phase transition.

The paper proceeds as follows. In Sec. II we introduce the formalism. Sec. III contains a brief description of a pedagogical implementation of the method which we provide as a supplement. Sec. IV contains results for temperature extrapolation, convergence acceleration, and first-order hysteresis. Finally, Sec. V contains our conclusions.

## II. METHOD

The central object of this paper is a causal matrix-valued fermionic Matsubara function which may represent a Green’s function, a self-energy, or a cumulant [34]. The Matsubara function is expressed as a three-dimensional tensor,  $G_{ij}(i\omega_n)$ , which associates a matrix (identified by the indices  $i$  and  $j$ ) with every Matsubara frequency  $\omega_n = (2n + 1)\pi/\beta$  ( $n$  denotes an integer,  $\beta$  the inverse temperature). Its continuation to the complex plane [33] is denoted as  $G_{ij}(\tilde{z})$ .  $iG(\tilde{z})$  is a Carathéodory function (up to a convention-dependent minus sign), such that  $[iG(\tilde{z}) + (iG(\tilde{z}))^\dagger]/2$  is a positive semi-definite matrix for any  $\tilde{z}$  in the upper half of the complex plane.

The matrix structure of  $G$  depends on the application. Matrices may be scalar, diagonal, block-diagonal, or fully dense. The scalar case typically appears in single-site single-orbital cases, such as single-site DMFT. The diagonal case is often encountered in momentum-space simulations, such as cluster DMFT [4–7]. The general multi-orbital case with dense matrices typically appears

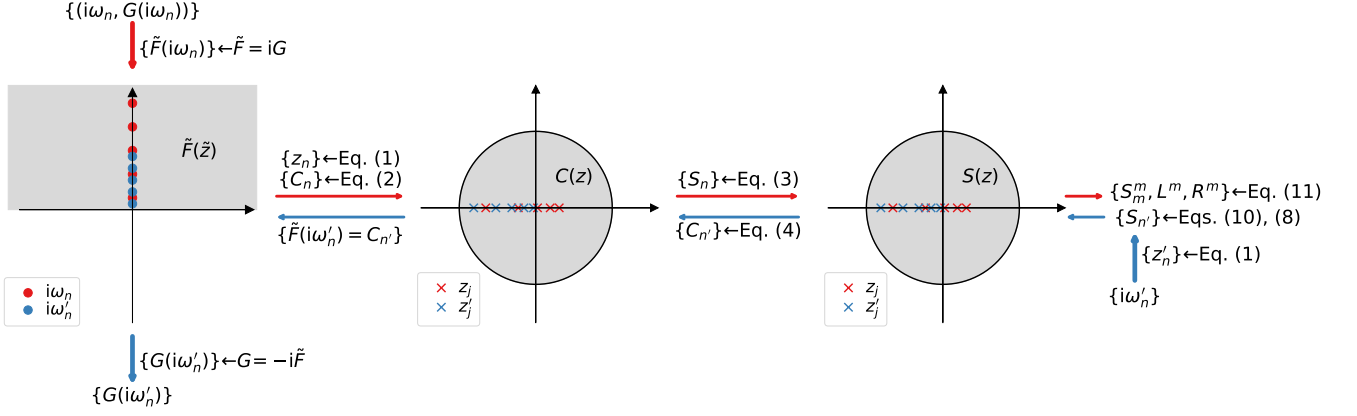


FIG. 1. Schematic representation of the interpolation procedure for a matrix-valued finite-temperature Matsubara function  $G(i\omega_n)$ . See text for detailed description.

in real-materials ab-initio calculations [25, 26].

The frequency-dependence of  $G$  is known at discrete Matsubara frequencies  $\omega_n$ . In the simplest case, the frequencies are uniformly spaced positive fermionic Matsubara frequencies  $\omega_n = (2n + 1)\pi/\beta$ ,  $n = 0, 1, \dots, N - 1$ . More generally, data is provided on a non-uniform frequency grid using Chebyshev [35], intermediate representation [36], Legendre [37], spline [38], or discrete Lehmann representation [39] schemes with associated Fourier transforms [40, 41]. Bosonic Matsubara response functions  $\Pi(\tilde{z})$  are not directly related to Carathéodory functions. However,  $\Pi(\tilde{z})\tilde{z}$  and  $\Pi(\tilde{z})/\tilde{z}^*$  correspond to Carathéodory functions [42], and Nogaki and Shinaoka [43] recently investigated a related mapping of bosonic functions.

Extrapolating in temperature requires the transformation of one Matsubara grid to another one corresponding to a different temperature. We propose to construct a causal matrix-valued interpolant through  $G(i\omega_n)$  and evaluating it at the Matsubara points corresponding to the changed temperature grid to realize the temperature extrapolation. The method's algorithmic steps follow those presented for analytic continuation in Ref. [33], with the only distinction that the interpolant is evaluated on the imaginary axis, rather than just above the real axis. The major steps of the algorithm are described below.

For a Carathéodory function  $\tilde{F}(\tilde{z}) = iG(\tilde{z})$ ,  $\tilde{z}$  in the upper half of the complex plane, we assume the values of  $\tilde{F}$  are known at a set of points  $\{\tilde{z}_n | n = 0, 1, \dots, N - 1\}$ . A Möbius transform

$$z = \frac{\tilde{z} - i}{\tilde{z} + i} \quad (1)$$

maps the upper half of the complex plane to the unit disk, the real axis to the unit circle, and the Matsubara points to points onto the real axis. Since a Carathéodory function  $F$  is a function defined on an open subset of the complex plane and exhibits the property

$(F + F^\dagger)/2$  being positive semi-definite,  $C(z) = \tilde{F}(\tilde{z})$  then defines a Carathéodory function on the unit disk  $|z| < 1$ . The function  $C(z)$  is known at a set of points  $\{z_n | n = 0, 1, \dots, N - 1\}$  with the values of

$$C_n \equiv C(z_n) = \tilde{F}(\tilde{z}_n). \quad (2)$$

The Cayley transform [44] and its inverse, defined as

$$S(z) = [I - C(z)][I + C(z)]^{-1}, \quad (3)$$

$$C(z) = [I + S(z)]^{-1}[I - S(z)], \quad (4)$$

map the Carathéodory function  $C(z)$  to a matrix-valued Schur function  $S(z)$  [45] and vice versa. A Schur function is defined as a function  $S(z)$  on the unit disk with the property  $\|S(z)\| \leq 1$ , where the matrix norm  $\|\cdot\|$  is defined as the largest singular value of  $S$ , or equivalently the largest eigenvalue of  $(SS^\dagger)^{1/2}$ .

The problem of interpolating the Carathéodory function  $C(z)$  is thus converted into the problem of determining an interpolant for the Schur function  $S(z)$ , where  $S(z)$  is known at  $N$  discrete points, given as  $S_n \equiv S(z_n)$ , with  $n = 0, 1, \dots, N - 1$ .

To identify the interpolant of the Schur function  $S(z)$ , we proceed to find a set of Schur functions  $S^0(z), S^1(z), \dots, S^m(z), \dots, S^N(z)$ , where each Schur function  $S^m(z)$  is known at  $N - m$  points  $z = z_m, z_{m+1}, \dots, z_{N-1}$  with the values of  $S_n^m \equiv S^m(z_n)$ .  $S^N(z)$  is an arbitrary Schur function without any constraints. We require  $S_n^0 = S_n$  such that  $S^0(z)$  serves as the desired interpolant for the Schur function  $S(z)$ .

To establish a connection between the two Schur functions  $S^m(z)$  and  $S^{m+1}(z)$ , a function  $B^m(z)$  is introduced, enabling a progressive determination of  $S^0(z)$  starting from  $S^N(z)$  [33]. The relationship between  $B^m(z)$  and  $S^m(z)$  is given by:

$$\frac{|z_m|(z_m - z)}{z_m(1 - z_m^*z)} B^m(z) = L^m[S^m(z) - S_m^m] \times [I - S_m^{m\dagger} S^m(z)]^{-1} R^m \quad (5)$$

with

$$L^m = [I - S_m^m S_m^{m\dagger}]^{-\frac{1}{2}}, \quad (6)$$

$$R^m = [I - S_m^{m\dagger} S_m^m]^{\frac{1}{2}}. \quad (7)$$

An equivalent form of this relation is

$$S^m(z) = [I + V^m(z) S_m^{m\dagger}]^{-1} [V^m(z) + S_m^m] \quad (8)$$

with

$$V^m(z) = \frac{|z_m|(z_m - z)}{z_m(1 - z_m^* z)} (L^m)^{-1} B^m(z) (R^m)^{-1}. \quad (9)$$

The relation between  $B^m(z)$  and  $S^{m+1}(z)$  reads

$$S^{m+1}(z) = [I - K^m K^{m\dagger}]^{-\frac{1}{2}} [B^m(z) - K^m] \cdot [I - K^{m\dagger} B^m(z)]^{-1} [I - K^{m\dagger} K^m]^{\frac{1}{2}}, \quad (10)$$

where  $K^m$  is an arbitrary matrix with  $\|K^m\| < 1$ .

The freedom in choosing arbitrary  $K^0, K^1, \dots, K^{N-1}$ , along with  $S^N(z)$ , allows for a full coverage of all possible interpolants for  $S(z)$ . The seemingly undetermined quantities in the aforementioned equations are the values of  $\{S_m^m \mid m = 0, 1, \dots, N-1\}$ . Starting from the given  $\{S_n^0 \mid n = 0, 1, \dots, N-1\}$ , as  $S_n^{m+1}$  are entirely determined by  $S_n^m$  and  $S_n^n$  by proceeding from Eq. (5) to Eq. (10), all  $S_m^m$  can be acquired in the process of calculating  $\{S_n^m \mid m = 0, 1, \dots, N-1; n = m, m+1, \dots, N\}$  from  $m = 0$  to  $m = N-1$ . After obtaining all  $S_m^m$  and the corresponding  $L^m$  and  $R^m$ , one can reverse the procedure, transitioning from Eq. (10) to Eq. (8), to compute  $S^m(z)$  from  $S^{m+1}(z)$  with a chosen  $S^N(z)$  as the starting point, until the desired interpolant  $S^0(z)$  is attained. Finally, an interpolant for  $C(z)$  can be derived using Eq. (4), and by multiplying  $-i$  and substituting  $z$  with  $\tilde{z}$  through the Möbius transform, the interpolant for  $G(\tilde{z})$  is obtained.

A sketch of the algorithm is shown in Fig. 1 (starting top left, following the arrows, terminating bottom left). In practice, we take  $\{\tilde{z}_n\} = \{i\omega_n \mid n = 0, 1, \dots, N-1\}$  along with the corresponding  $G(i\omega_n)$  as the input where  $\omega_n = (2n+1)\pi/\beta$ . Setting  $\tilde{F} = iG$ , and with Eqs. (1), (2), and (3), we obtain the constraints  $\{(z_n, S_n)\}$  for the interpolation problem of a Schur function  $S(z)$ . By taking  $K^m = 0$  for all  $m$ s, from Eq.(10), we obtain  $S^{m+1}(z) = B^m(z)$  which leads to

$$S_n^{m+1} = \frac{z_m(1 - z_m^* z_n)}{|z_m|(z_m - z_n)} L^m [S_n^m - S_m^m] [I - S_m^{m\dagger} S_n^m]^{-1} R^m \quad (11)$$

according to Eq. (5). This equation offers a concrete way to calculate all  $S_n^m$ , starting from  $S_n^0 = S_n$ . Subsequently, we can obtain  $S_m^m$  and the corresponding  $L^m$  and  $R^m$ . Assume the desired new Matsubara points for a different temperature  $\beta'$  are  $i\omega'_n = i(2n+1)\pi/\beta'$ . Using the Möbius transform, the corresponding points in the domain of  $S(z)$  are obtained as  $z'_n$ . By setting  $S^N(z) = I$ , and using the obtained  $\{S_m^m, L^m, R^m\}$ , the

values of  $S_{n'} \equiv S^0(z'_n)$  can be determined by proceeding from Eq. (10) to Eq. (8). With the inverse Cayley transform in Eq. (4) and  $G = -i\tilde{F}$ , the desired values of the causal interpolant  $G(i\omega'_n)$  at  $i\omega'_n$  are obtained as output.

### III. IMPLEMENTATION

We provide a straightforward pedagogical implementation of the algorithm as supplement to this paper [46]. The code is written in the `python` programming language, using no dependencies other than `numpy`. Unlike related real-frequency analytic continuation codes [33, 47], we found that an implementation in standard double precision was sufficient to perform all calculations, and that the temperature extrapolation of noisy Monte Carlo data presented no difficulties.

The implementation requires a Green's function (or, equivalently, self-energy or cumulant)  $G[n, i, j] = G_{ij}(i\omega_n)$  as a three-dimensional tensor and  $w[n] = i\omega_n$  as a one-dimensional vector. After reading the data, all preprocessing steps indicated by the red arrows in Fig. 1 are performed, and  $\{S_m^m, L^m, R^m\}$  are obtained and stored.

The code also requires a set of frequencies  $wp[n] = i\omega'_n$ , provided as a one-dimensional vector. These frequencies should correspond to the Matsubara points at the new temperature  $\beta'$ . Using this data, the code evaluates the interpolated Green's function at the new Matsubara points, according to the blue arrows in Fig. 1 and returns  $G[n', i, j] = G_{ij}(i\omega'_n)$  as a three-dimensional tensor.

The supplemental materials contain detailed instructions and usage examples for the code.

### IV. RESULTS

We showcase results for the temperature extrapolation technique applied to a range of typical self-consistent finite-temperature methods. Sec. IV A investigates the accuracy and convergence properties of the extrapolation technique. Sec. IV B examines the convergence acceleration resulting from an enhanced starting point provided by the extrapolation technique. This study is conducted specifically within the context of single-site DMFT and cluster DMFT calculations for the Hubbard model, as well as the self-consistent GW approximation for nickel oxide (NiO) real material calculations. Sec. IV C demonstrates the occurrence of hysteresis during heating and cooling processes at a first-order phase transition, utilizing the extrapolation technique.

#### A. Temperature extrapolation

In this section, we provide an illustration of temperature extrapolation in a cluster DMFT [7] calculation, as depicted in Figure 2. Specifically, we present the self-energy at the antinodal point,  $(\pi, 0)$ , for a simulation of

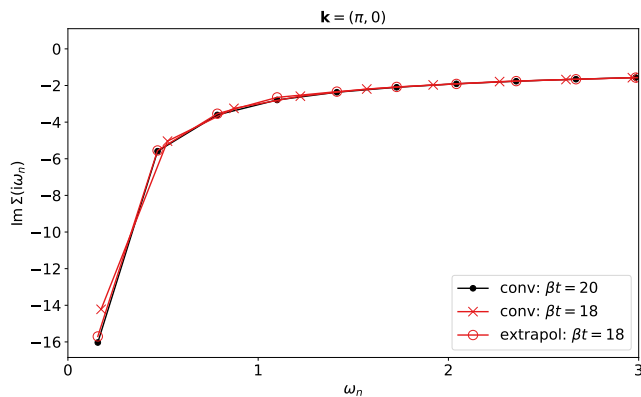


FIG. 2. Imaginary part of a cluster DMFT [7] self-energy,  $\text{Im}\Sigma(i\omega_n)$ , as a function of  $\omega_n$  for the 2D Hubbard model at the antinodal point  $(\pi, 0)$  with  $U = 6t$  (see text for calculation setup). Converged data at  $\beta t = 18$  (red crosses) and  $\beta t = 20$  (black dots) along with temperature extrapolation (red circle) from  $\beta t = 18$  to  $\beta t = 20$ . The labels of the extrapolation results indicate the initial inverse temperature used for extrapolation.

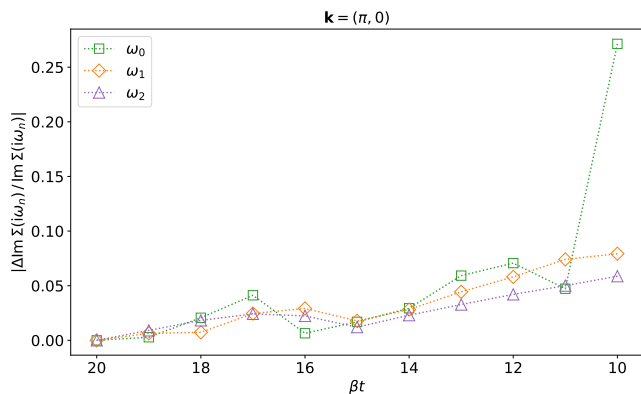


FIG. 3. Difference  $|\Delta\text{Im}\Sigma(i\omega_n)/\text{Im}\Sigma(i\omega_n)|$  between the converged self-energy at  $\beta t = 20$  and the extrapolation from the converged self-energy at higher temperature, shown as a function of the extrapolation inverse temperature for the three lowest Matsubara frequencies  $\omega_n$ , with  $n = 0, 1, 2$  (see text for calculation setup).

the two-dimensional Hubbard model [48]. The simulation was performed on a 16-site ( $4 \times 4$ ) cluster, and the continuous-time auxiliary field impurity solver [49, 50] was employed. The system was solved at half-filling, in the paramagnetic state, with no next-nearest neighbor hopping, and at an interaction strength of  $U = 6t$ , which corresponds to a Mott insulating regime. The self-energy in this regime exhibits a strong temperature dependence, and various phases such as metallic, insulating, superconducting, and pseudo-gapped phases are in close proximity [31, 51, 52]. For a comprehensive discussion of the physics of this self-energy, we refer the reader to the extensive literature on this system, including the reviews [7, 48] and references therein.

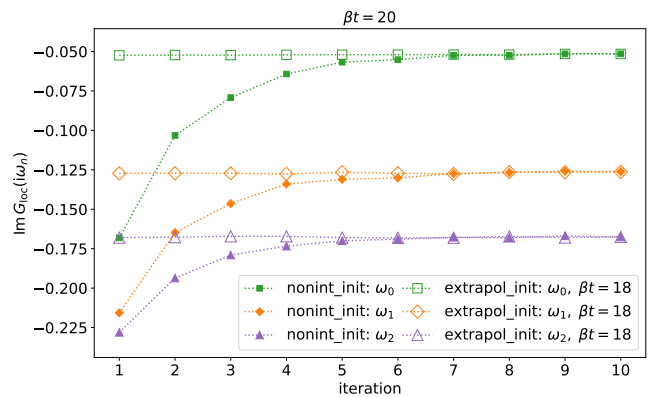


FIG. 4. Cluster DMFT convergence of the imaginary part of the local Green's function  $G_{\text{loc}}$  as a function of iteration for the three lowest Matsubara frequencies at  $\beta t = 20$  (see text for calculation setup). Convergence to the fixed point is shown for the non-interacting starting point (filled symbols) and the starting point extrapolated from the converged solution at  $\beta t = 18$  (open symbols). The labels of the extrapolation results indicate the initial inverse temperature used for extrapolation.

Fig. 2 presents the fully converged, self-consistent imaginary part of the self-energy,  $\Sigma(i\omega_n)$ , at  $\beta t = 18$  (red crosses) and at  $\beta t = 20$  (black dots). Red circles illustrate the extrapolation of the  $\beta = 18t$  self-energy to  $\beta = 20t$  using the Carathéodory formalism. The extrapolated data aligns with the converged points for all frequency points, except for the lowest one. The discrepancy between converged data and extrapolation data at  $\beta = 20t$  serves as an indicator of additional correlations emerging in the system as it cools down.

Fig. 3 demonstrates the deviation of the extrapolated self-energy at the three lowest Matsubara frequencies at  $\beta t = 20$ . The extrapolation is conducted using converged data at  $\beta t = 10, 11, \dots, 19$ . Notably, while the lowest frequency of the self-energy exhibits significant deviations when extrapolated by a factor of two from  $\beta t = 10$  to  $\beta t = 20$ , these deviations rapidly diminish if the extrapolation interval (the difference between the initial temperature and targeted temperature) is reduced.

Figs. 2 and 3 demonstrate that the Carathéodory structure of many-body functions can be effectively utilized to extrapolate data in temperature.

## B. Starting point and Convergence

### 1. Convergence of the extrapolated starting point away from phase transitions

A temperature extrapolation of this type can be used to improve the starting point for the convergence of self-consistent many-body methods, such as DMFT [28, 53, 54] and its cluster extensions [4–7]. The DMFT equations are solved using a fixed-point iteration scheme, in

which an initial estimate of the self-energy (commonly chosen as  $\Sigma(i\omega_n) \equiv 0$ ) serves as an initial guess for the iteration. The equations typically converge rapidly if the initial starting point of the iteration is near the stationary point. Since the computational effort is proportional to the number of iterations required, a starting point closer to the stationary point reduces the calculation time.

Fig. 4 displays the imaginary part of the lowest three frequencies of the local Green's function,  $G_{\text{loc}}(i\omega_n)$ , for a typical cluster DMFT calculation away from phase transitions, using non-interacting starting points (filled symbols) and starting points derived from temperature extrapolation (open symbols), as a function of iteration. The calculation setup is identical to the one in Sec. IV A (a 16-site cluster in the paramagnetic state with  $\beta t = 20$ ,  $U = 6t$ , and at half filling). A naive non-interacting starting point converges in approximately seven iterations. Moreover, a few additional iterations are necessary to confirm that convergence has been achieved. In contrast, a starting point generated by extrapolating from higher to lower temperatures almost immediately yields a converged result.

## 2. DMFT convergence near a phase transition

Self-consistent many-body methods are notoriously slow to converge in the vicinity of phase transitions. This can be illustrated at the example of a single-site DMFT calculation on an infinite coordination number Bethe lattice with bandwidth  $W = 4t$ . The single-site DMFT calculation exhibits a first-order phase transition between a paramagnetic metal at weak interaction and low temperature and a paramagnetic Mott insulator at large interaction and higher temperature [54–60], as depicted in the inset of Fig. 5. At an interaction strength  $U = 4.7t$ , the system is insulating at high temperature, metallic at low temperature, and both metallic and insulating solutions coexist in an intermediate temperature regime. We show the convergence of the imaginary-time Green's function in the middle of the imaginary time interval,  $-G(\beta/2)$ , in Fig. 5, which is related to the spectral density at the Fermi surface in the low-temperature limit as  $A(\omega = 0) \sim -\beta G(\beta/2)$ , at temperatures close to the two boundaries of the coexistence region.

At a temperature of  $\beta t = 20.31$ , the system exhibits Mott insulating behavior. The upper panel of Fig. 5 shows that hundreds of iterations are required to achieve convergence when initiating from the non-interacting limit (black dots). Similarly, starting with an extrapolation from a lower temperature metallic solution in the coexistence region (blue circles) results in slow convergence toward the insulating fixed point. Conversely, the extrapolation from a higher temperature insulating phase converges rapidly (red circles). A starting point derived from the atomic limit also leads to relatively fast convergence (gray dots).

Conversely, at a temperature of  $\beta t = 21.56$  (Fig. 5

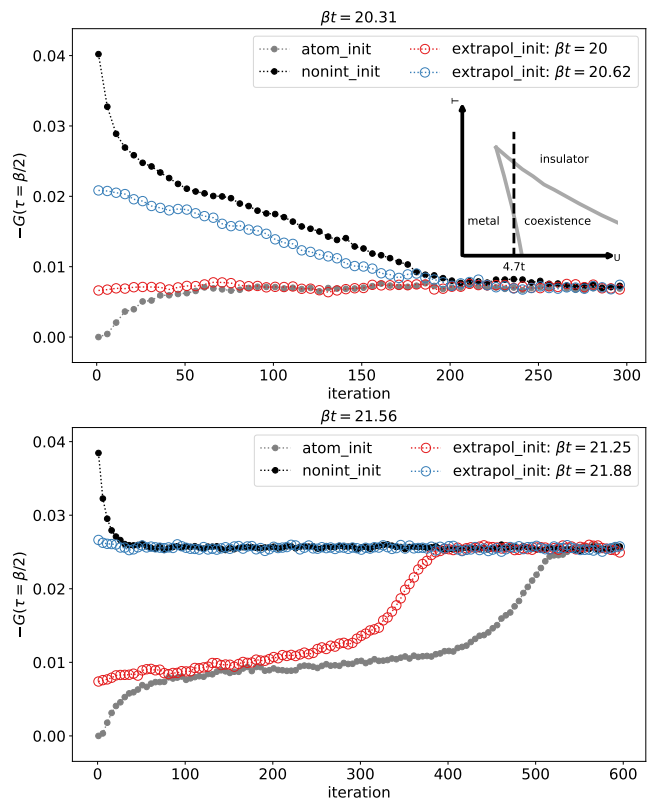


FIG. 5. DMFT convergence of  $-G(\beta/2)$  on a half-filled infinite-coordination Bethe lattice with  $U = 4.7t$  and bandwidth  $W = 4t$  as a function of iteration. The top and lower panels display the insulating ( $\beta t = 20.31$ ) and metallic ( $\beta t = 21.56$ ) phases, respectively. Atomic starting point: gray dots. Non-interacting starting point: black dots. Extrapolated starting points: red circles and blue circles. Inset: phase diagram adapted from Ref. [55]. The labels of the extrapolation results indicate the initial inverse temperature used for extrapolation.

lower panel), the system is in a metallic state. Convergence from an ‘insulating’ starting point requires hundreds of iterations to reach convergence (red circles for the starting point extrapolated from a higher temperature insulating solution, and gray dots for the atomic limit starting point). Convergence from a metallic solution, like the non-interacting limit solution (black dots), is substantially faster, and a starting point extrapolated from a converged metallic solution at lower temperature leads to even faster convergence (blue circles).

Fig. 5 therefore shows that even though all starting points, including atomic, non-interacting, and extrapolated, converge to the identical solution, extrapolation efficiently accelerates convergence, provided that the extrapolated solution is in the same phase as the solution at the target temperature. For extrapolation originating from a different phase (at the boundary of phase transitions, solutions with distinct properties become possible for two neighboring temperatures), the extrapolated starting points still perform better than the sim-

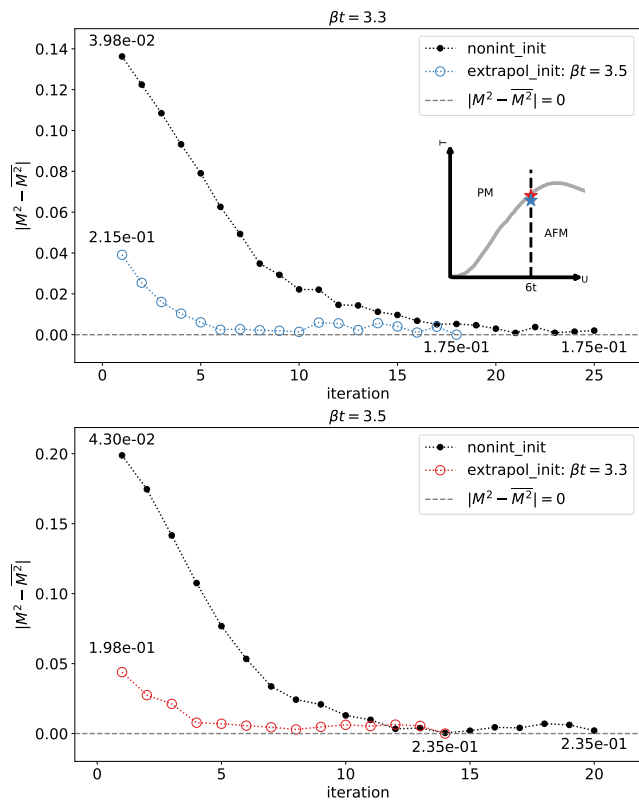


FIG. 6. Cluster DMFT convergence of the squared magnetic moment on the half-filled 3D Hubbard model (using a 34-site cluster with a doubled unit cell) at  $U = 6t$  and  $\beta t = 3.3$  (upper panel) and 3.5 (lower panel) as a function of iteration. Dots: non-interacting starting point. Circles: temperature extrapolation. Inset: phase diagram adapted from Ref. [61].  $M^2$  at the first and last iteration indicated by numbers.  $\bar{M}^2$  corresponds to the values at the last iteration of red or blue circles, which serves as a reference for converged values. The labels of the extrapolation results indicate the initial inverse temperature used for extrapolation.

plistic starting points corresponding to the ‘wrong’ phase, specifically, the non-interacting solution or the atomic solution.

### 3. Cluster DMFT convergence near a phase transition

At second order phase transitions, critical slowing down, rather than coexistence and hysteresis, is expected. This phenomenon leads to a slow convergence of the fixed point iteration. We illustrate this at the example of a half-filled three-dimensional Hubbard model treated within cluster DMFT [62–64], calculated on a 34-site cluster with a doubled unit cell. This model exhibits a phase transition between a paramagnetic (PM) state at high temperature and an antiferromagnetic (AFM) insulator at low temperature, as depicted in the inset of Fig. 6. The model has been studied extensively within

the context of ultracold atomic gases. In Fig. 6, we examine two points,  $\beta t = 3.3$  and  $\beta t = 3.5$ , in the ordered phase at  $U = 6t$ , near the AFM phase transition (the critical point is at about  $\beta t = 2.7$ ). A starting point from temperature extrapolation cannot completely overcome the slowing down (since the self-energy itself exhibits strong temperature dependence) but does lead to an acceleration of the convergence by at least a factor of two, as illustrated by the convergence of the squared magnetic moment shown in Fig. 6.

### 4. GW convergence of realistic many-body simulations

Finally, we turn to realistic simulations within a weak-coupling framework. We show examples for periodic solid NiO treated within the so-called GW approximation [8–13]. The GW approximation takes into account screening processes via a renormalized, frequency-dependent interaction, but neglects the second-order exchange diagram. It is therefore mostly used for weakly correlated systems such as semiconductors. In the calculation for NiO, a  $4 \times 4 \times 4$  cluster with a doubled unit cell along the  $[1, 1, 1]$  direction and a fixed lattice constant  $a = 4.1705 \text{ \AA}$  [65] is utilized. The *gth-dzvp-molopt-sr* basis [66] along with the *gth-pbe* pseudopotential [3] is employed. For the density fitting of Coulomb integrals, the *def2-svp-ri* basis set is chosen as the auxiliary basis [67]. Finite-size errors in the GW exchange diagram are corrected using the Ewald probe-charge approach [68, 69]. The Coulomb integrals and non-interacting matrix elements are obtained from PYSCF [70]. In order to decrease the number of frequencies utilized in the computation, the intermediate representation grid [36] is employed. A comprehensive description of the methods and implementation, in conjunction with the computational setup for evaluating NiO, is extensively detailed in Refs. [12, 71].

When applied to the antiferromagnetic materials NiO, the GW method shows a continuous transition to an ordered state with a non-zero staggered magnetization at low temperature. Within the GW framework, the transition temperature is situated near  $\beta = 25 \text{ Ha}^{-1}$ . As illustrated in Fig. 7, the convergence to this ordered state, initiated from an unrestricted Hartree-Fock solution (black dots), is relatively slow. This is evident in the convergence of both the squared magnetic moment for Ni and the total energy. However, when starting from extrapolated starting points (blue or red circles), the convergence occurs at a significantly faster pace, with an initial starting point akin to iteration 30 of the Hartree-Fock-initialized convergence.

At considerably lower temperatures, deep within the AFM phase, the extrapolation of the self-energy results in a starting point that is essentially exact because the self-energy is only weakly temperature-dependent, similar to the 2D Hubbard model case shown at the beginning of Sec. IV B. Fig. 8 displays the temperature extrapolation from  $\beta t = 100$  to  $\beta t = 200$ , and vice versa, in comparison

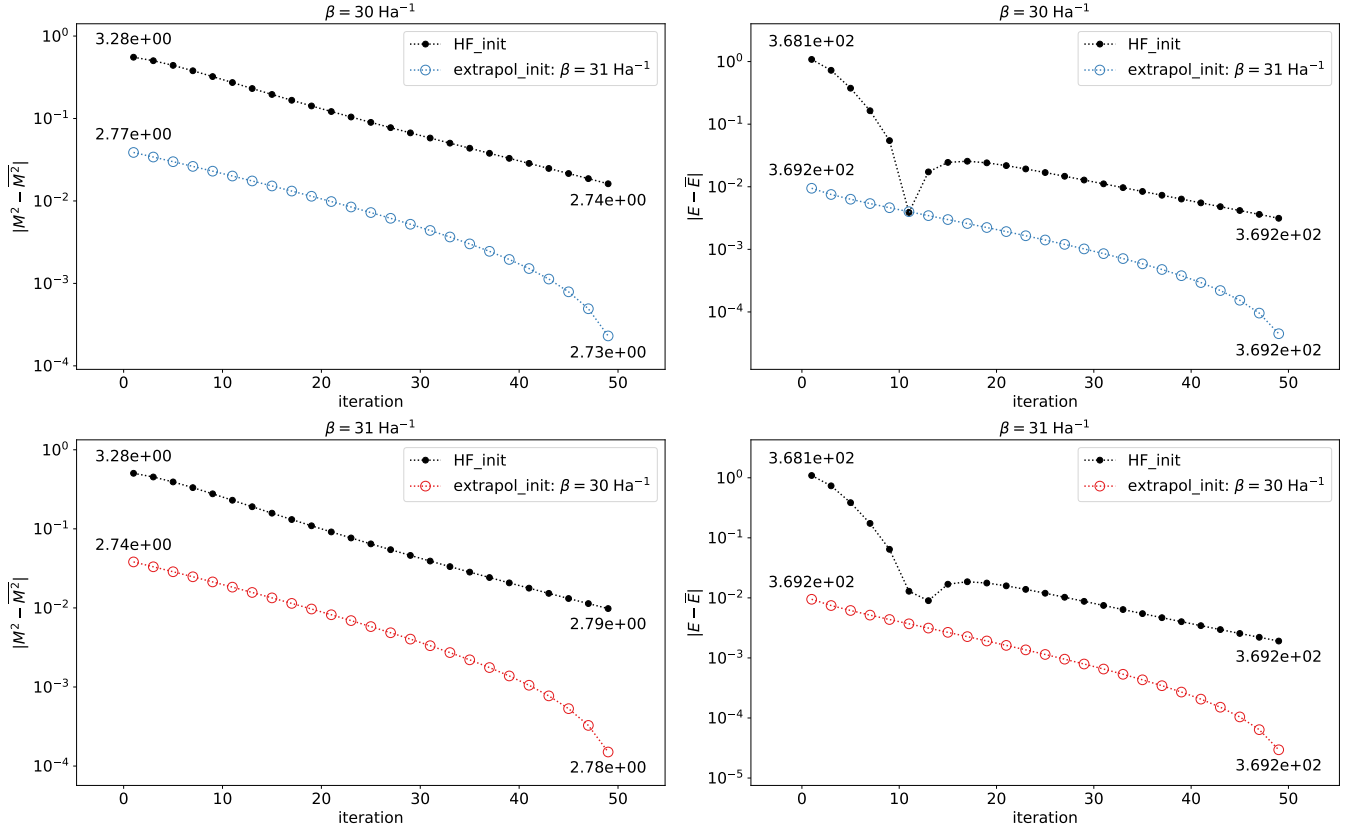


FIG. 7. GW convergence of the squared magnetic moment (left) and energy (right) near the AFM phase transition of NiO at  $\beta = 30 \text{ Ha}^{-1}$  (upper panel) and  $\beta = 31 \text{ Ha}^{-1}$  (lower panel) as a function of iteration. Calculations with unrestricted Hartree-Fock self-energy starting point are represented by black dots, while calculations with temperature-extrapolated self-energy are denoted by red circles (indicating extrapolation from higher temperature solutions) or blue circles (indicating extrapolation from lower temperature solutions). The values of  $M^2$  and  $E$  at the first and last iterations are indicated by the numbers. The values of  $\bar{M}^2$  and  $\bar{E}$  are determined as the values at the last iteration of red or blue circles. The Hartree atomic units are used. The labels of the extrapolation results indicate the initial inverse temperature used for extrapolation.

with the Hartree-Fock starting points.

### C. Heating and Cooling

The possibility of obtaining a starting point for fixed-point iteration by extrapolating from a nearby temperature point allows to smoothly change temperature in subsequent simulation, in analogy to ‘heating’ and ‘cooling’ measurements in experiments. This capability is especially important at first-order phase transitions, where multiple stable fixed points, corresponding to the different phases, exist.

Such a heating and cooling process is shown in Fig. 9. Shown is a coexistence region and hysteresis curve at the example of the single-site DMFT on a Bethe lattice (the same calculation setup as the one mentioned in Sec. IV B). We plot the double occupancy, which is directly related to the potential energy, as a function of inverse temperature  $\beta$ . With starting points extrapolated from higher temperature converged results (red open cir-

cles), we find a transition from an insulating phase with small double-occupancy to a metallic phase with large double-occupancy around  $\beta t = 21.56$ . Conversely, with starting points extrapolated from lower temperature converged results (blue open circles), we find a transition from a metallic phase to an insulating phase around  $\beta t = 20.31$ . Between those temperatures, both metal and insulator are stable solutions of the fixed-point equations, indicating phase coexistence [54–60, 72].

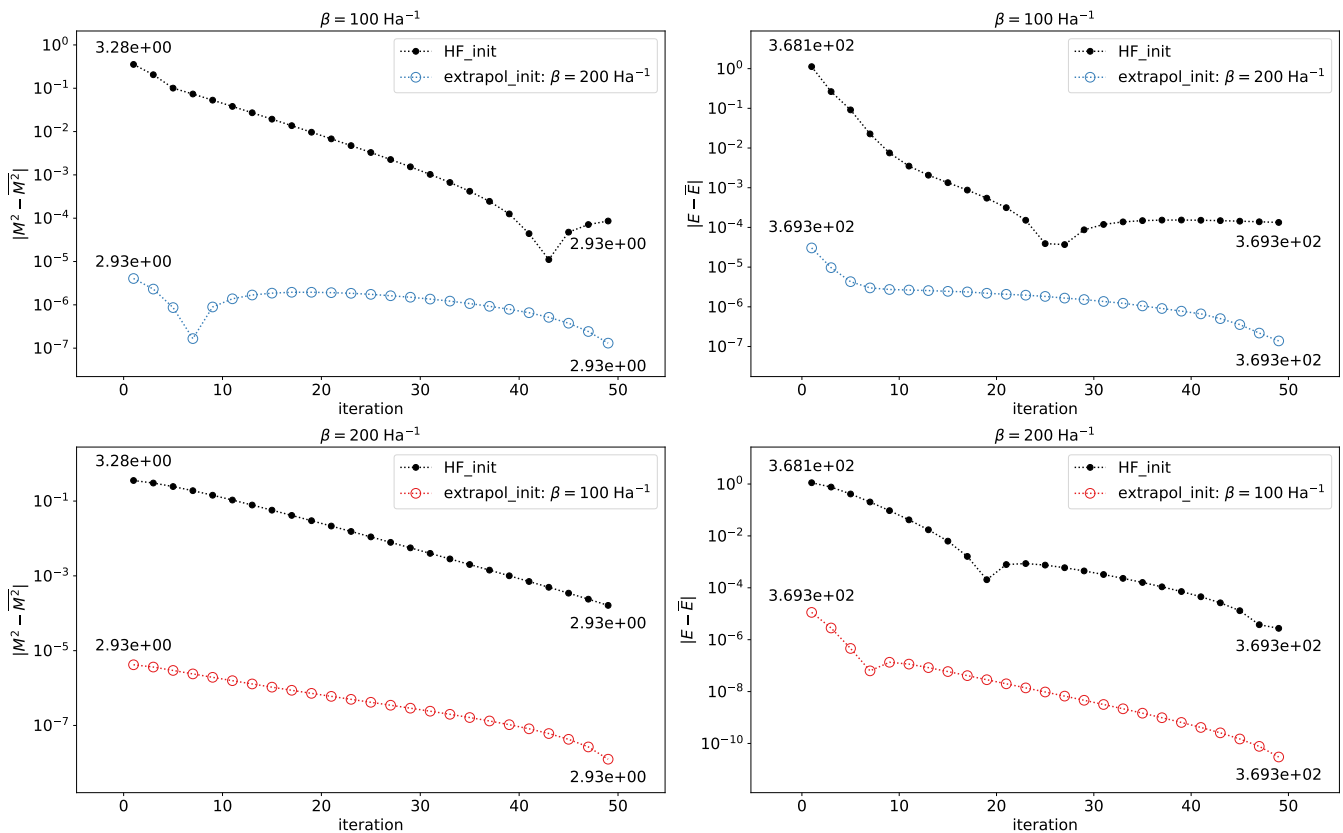


FIG. 8. GW convergence of the squared magnetic moment (left) and energy (right) deep within the AFM phase of NiO at  $\beta = 100 \text{ Ha}^{-1}$  (upper panel) and  $\beta = 200 \text{ Ha}^{-1}$  (lower panel) as a function of iteration. Calculations with unrestricted Hartree-Fock self-energy starting point are represented by black dots, while calculations with temperature-extrapolated self-energy are denoted by red circles (indicating extrapolation from higher temperature solutions) or blue circles (indicating extrapolation from lower temperature solutions). The values of  $M^2$  and  $E$  at the first and last iterations are indicated by the numbers. The values of  $\bar{M}^2$  and  $\bar{E}$  are determined as the values at the last iteration of red or blue circles. The Hartree atomic units are used. The labels of the extrapolation results indicate the initial inverse temperature used for extrapolation.

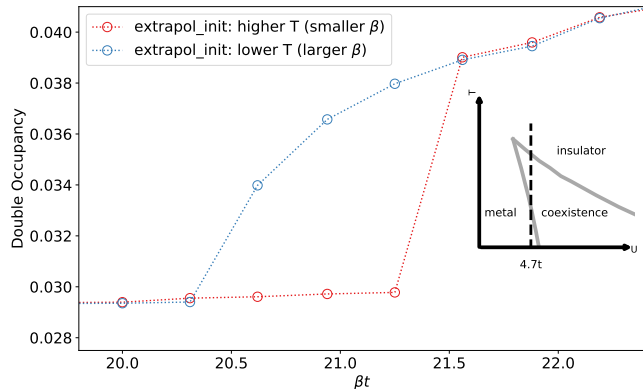


FIG. 9. DMFT analysis of a half-filled Bethe lattice with  $U = 4.7t$  and a bandwidth of  $4t$ , displaying the hysteresis near  $\beta t = 21$ . Points on the red curve utilize extrapolation from the nearest higher temperature converged results as the starting points for the calculation, while points on the blue curve employ extrapolation from the nearest lower temperature converged results as the starting points for the calculation. Inset: phase diagram adapted from Ref. [55].

## V. CONCLUSIONS

The Carathéodory temperature extrapolation technique, introduced in this paper, provides an effective way to accelerate the convergence of self-consistent many-body calculations for both model Hamiltonians and realistic systems. It allows for smooth temperature variation in simulations, making it suitable for studying heating and cooling processes in many-body systems. The starting points provided by this method are generally superior, especially in systems with phase transitions and convergence issues. The Carathéodory technique therefore offers a versatile and efficient approach for studying temperature-dependent properties in self-consistent many-body calculations that should be adapted in any self-consistent finite-temperature many-body simulation.

We note that ‘convergence acceleration’ techniques such as DIIS [73–75] and Anderson acceleration [76–79] are complementary to the Carathéodory temperature extrapolation method employed in this study. Convergence acceleration techniques work by extrapolating from a set



of initial iterations. The combination of such techniques with the better starting points provided by Carathéodory temperature extrapolation is therefore straightforward.

### ACKNOWLEDGMENTS

We thank André Erpenbeck for helpful discussions. This material is based upon work supported by the Na-

tional Science Foundation under Grant No. NSF DMR 2001465. Real material calculations used resources of the National Energy Research Scientific Computing Center, a DOE Office of Science User Facility supported by the Office of Science of the U.S. Department of Energy under Contract No. DE-AC02-05CH11231 using NERSC award BES-ERCAP0023196.

- 
- [1] A. A. Abrikosov, L. P. Gor'kov, and I. E. Dzialoshinskiĭ, *Methods of quantum field theory in statistical physics*, rev. english ed ed. (Dover Publications, New York, 1975).
- [2] G. D. Mahan, *Many-Particle Physics*, 3rd ed., Physics of Solids and Liquids (Kluwer Academic/Plenum Publishers, New York, 2000).
- [3] S. Goedecker, M. Teter, and J. Hutter, *Physical Review B* **54**, 1703 (1996).
- [4] M. H. Hettler, A. N. Tahvildar-Zadeh, M. Jarrell, T. Pruschke, and H. R. Krishnamurthy, *Physical Review B* **58**, R7475 (1998).
- [5] A. I. Lichtenstein and M. I. Katsnelson, *Physical Review B* **62**, R9283 (2000).
- [6] G. Kotliar, S. Y. Savrasov, G. Pálsson, and G. Biroli, *Physical Review Letters* **87**, 186401 (2001).
- [7] T. Maier, M. Jarrell, T. Pruschke, and M. H. Hettler, *Reviews of Modern Physics* **77**, 1027 (2005).
- [8] L. Hedin, *Physical Review* **139**, A796 (1965).
- [9] F. Aryasetiawan and O. Gunnarsson, *Reports on Progress in Physics* **61**, 237 (1998).
- [10] A. Kutepov, S. Y. Savrasov, and G. Kotliar, *Physical Review B* **80**, 041103 (2009).
- [11] A. L. Kutepov, *Computer Physics Communications* **257**, 107502 (2020).
- [12] C.-N. Yeh, S. Isakov, D. Zgid, and E. Gull, *Physical Review B* **106**, 235104 (2022).
- [13] C.-N. Yeh, A. Shee, Q. Sun, E. Gull, and D. Zgid, *Physical Review B* **106**, 085121 (2022).
- [14] N. E. Dahlen and R. van Leeuwen, *The Journal of Chemical Physics* **122**, 164102 (2005).
- [15] J. J. Phillips and D. Zgid, *The Journal of Chemical Physics* **140**, 241101 (2014).
- [16] A. A. Rusakov and D. Zgid, *The Journal of Chemical Physics* **144**, 054106 (2016).
- [17] S. Isakov, A. A. Rusakov, D. Zgid, and E. Gull, *Physical Review B* **100**, 085112 (2019).
- [18] N. E. Bickers, D. J. Scalapino, and S. R. White, *Physical Review Letters* **62**, 961 (1989).
- [19] S. Isakov and E. Gull, *Physical Review B* **105**, 045109 (2022).
- [20] N. Prokof'ev and B. Svistunov, *Physical Review Letters* **99**, 250201 (2007).
- [21] E. Gull, D. R. Reichman, and A. J. Millis, *Physical Review B* **82**, 075109 (2010).
- [22] E. Gull, D. R. Reichman, and A. J. Millis, *Physical Review B* **84**, 085134 (2011).
- [23] G. Cohen, D. R. Reichman, A. J. Millis, and E. Gull, *Physical Review B* **89**, 115139 (2014).
- [24] S. Biermann, F. Aryasetiawan, and A. Georges, *Physical Review Letters* **90**, 086402 (2003).
- [25] G. Kotliar, S. Y. Savrasov, K. Haule, V. S. Oudovenko, O. Parcollet, and C. A. Marianetti, *Reviews of Modern Physics* **78**, 865 (2006).
- [26] D. Zgid and E. Gull, *New Journal of Physics* **19**, 023047 (2017).
- [27] E. Kozik, M. Ferrero, and A. Georges, *Physical Review Letters* **114**, 156402 (2015).
- [28] A. Georges, G. Kotliar, W. Krauth, and M. J. Rozenberg, *Reviews of Modern Physics* **68**, 13 (1996).
- [29] G. Kotliar and D. Vollhardt, *Physics Today* **57**, 53 (2004).
- [30] A. Macridin, M. Jarrell, and Th. Maier, *Physical Review B* **74**, 085104 (2006).
- [31] E. Gull, O. Parcollet, P. Werner, and A. J. Millis, *Physical Review B* **80**, 245102 (2009).
- [32] C. Walsh, P. Sémon, D. Poulin, G. Sordi, and A.-M. S. Tremblay, *Physical Review Letters* **122**, 067203 (2019).
- [33] J. Fei, C.-N. Yeh, D. Zgid, and E. Gull, *Physical Review B* **104**, 165111 (2021).
- [34] T. D. Stanescu and G. Kotliar, *Physical Review B* **74**, 125110 (2006).
- [35] E. Gull, S. Isakov, I. Krivenko, A. A. Rusakov, and D. Zgid, *Physical Review B* **98**, 075127 (2018).
- [36] H. Shinaoka, J. Otsuki, M. Ohzeki, and K. Yoshimi, *Physical Review B* **96**, 035147 (2017).
- [37] L. Boehnke, H. Hafermann, M. Ferrero, F. Lechermann, and O. Parcollet, *Physical Review B* **84**, 075145 (2011).
- [38] A. A. Kananenka, A. R. Welden, T. N. Lan, E. Gull, and D. Zgid, *Journal of Chemical Theory and Computation* **12**, 2250 (2016).
- [39] J. Kaye, K. Chen, and O. Parcollet, *Physical Review B* **105**, 235115 (2022).
- [40] J. Li, M. Wallerberger, N. Chikano, C.-N. Yeh, E. Gull, and H. Shinaoka, *Physical Review B* **101**, 035144 (2020).
- [41] M. Kaltak and G. Kresse, *Physical Review B* **101**, 205145 (2020).
- [42] J. Fei, *A Probe into Propagators*, Thesis (2021).
- [43] K. Nogaki and H. Shinaoka, *Journal of the Physical Society of Japan* **92**, 035001 (2023).
- [44] A. Cayley, **1846**, 119 (1846).
- [45] J. Schur, *Journal für die reine und angewandte Mathematik* **148**, 122 (1918).
- [46] See Supplemental Material at [URL will be inserted by publisher] for Python implementation of the algorithm, documentation, and examples.
- [47] J. Fei, C.-N. Yeh, and E. Gull, *Physical Review Letters* **126**, 056402 (2021).
- [48] M. Qin, T. Schäfer, S. Andergassen, P. Corboz, and

- E. Gull, Annual Review of Condensed Matter Physics **13**, 275 (2022).
- [49] E. Gull, P. Werner, O. Parcollet, and M. Troyer, Europhysics Letters **82**, 57003 (2008).
- [50] E. Gull, A. J. Millis, A. I. Lichtenstein, A. N. Rubtsov, M. Troyer, and P. Werner, Reviews of Modern Physics **83**, 349 (2011).
- [51] P. Werner, E. Gull, O. Parcollet, and A. J. Millis, Physical Review B **80**, 045120 (2009).
- [52] E. Gull, M. Ferrero, O. Parcollet, A. Georges, and A. J. Millis, Physical Review B **82**, 155101 (2010).
- [53] W. Metzner and D. Vollhardt, Physical Review Letters **62**, 324 (1989).
- [54] A. Georges and G. Kotliar, Physical Review B **45**, 6479 (1992).
- [55] N. Blümer, *Mott-Hubbard metal insulator transition and optical conductivity in high dimensions*, Ph.D. thesis, Universität Augsburg (2003).
- [56] M. Jarrell, Physical Review Letters **69**, 168 (1992).
- [57] M. J. Rozenberg, X. Y. Zhang, and G. Kotliar, Physical Review Letters **69**, 1236 (1992).
- [58] X. Y. Zhang, M. J. Rozenberg, and G. Kotliar, Physical Review Letters **70**, 1666 (1993).
- [59] M. J. Rozenberg, R. Chitra, and G. Kotliar, Physical Review Letters **83**, 3498 (1999).
- [60] R. Bulla, Physical Review Letters **83**, 136 (1999).
- [61] R. Staudt, M. Dzierzawa, and A. Muramatsu, The European Physical Journal B - Condensed Matter and Complex Systems **17**, 411 (2000).
- [62] P. R. C. Kent, M. Jarrell, T. A. Maier, and Th. Pruschke, Physical Review B **72**, 060411 (2005).
- [63] S. Fuchs, E. Gull, L. Pollet, E. Burovski, E. Kozik, T. Pruschke, and M. Troyer, Physical Review Letters **106**, 030401 (2011).
- [64] S. Fuchs, E. Gull, M. Troyer, M. Jarrell, and T. Pruschke, Physical Review B **83**, 235113 (2011).
- [65] L. C. Bartel and B. Morosin, Physical Review B **3**, 1039 (1971).
- [66] J. VandeVondele and J. Hutter, The Journal of Chemical Physics **127**, 114105 (2007).
- [67] C. Hättig, Physical Chemistry Chemical Physics **7**, 59 (2005).
- [68] J. Paier, R. Hirschl, M. Marsman, and G. Kresse, The Journal of Chemical Physics **122**, 234102 (2005).
- [69] R. Sundararaman and T. A. Arias, Physical Review B **87**, 165122 (2013).
- [70] Q. Sun, T. C. Berkelbach, N. S. Blunt, G. H. Booth, S. Guo, Z. Li, J. Liu, J. D. McClain, E. R. Sayfutyarova, S. Sharma, S. Wouters, and G. K.-L. Chan, WIREs Computational Molecular Science **8**, e1340 (2018).
- [71] S. Iskakov, C.-N. Yeh, E. Gull, and D. Zgid, Physical Review B **102**, 085105 (2020).
- [72] A. Erpenbeck, W.-T. Lin, T. Blommel, L. Zhang, S. Iskakov, L. Bernheimer, Y. Núñez-Fernández, G. Cohen, O. Parcollet, X. Waintal, and E. Gull, A Tensor Train Continuous Time Solver for Quantum Impurity Models (2023), arxiv:2303.11199 [cond-mat].
- [73] P. Pulay, Chemical Physics Letters **73**, 393 (1980).
- [74] P. Pulay, Journal of Computational Chemistry **3**, 556 (1982).
- [75] P. Pokhilko, C.-N. Yeh, and D. Zgid, The Journal of Chemical Physics **156**, 094101 (2022).
- [76] G. B. Bacskay, Chemical Physics **61**, 385 (1981).
- [77] H. F. Walker and P. Ni, SIAM Journal on Numerical Analysis **49**, 1715 (2011).
- [78] C. Evans, S. Pollock, L. G. Rebholz, and M. Xiao, SIAM Journal on Numerical Analysis **58**, 788 (2020).
- [79] S. Pollock and L. G. Rebholz, IMA Journal of Numerical Analysis **41**, 2841 (2021).